AIAA JOURNAL
Vol. 34, No. 12, December 1996

Nonlinear Analysis of Pressurized Spinning Fiber-Reinforced Tori

Raouf A. Raouf*
U.S. Naval Academy, Annapolis, Maryland 21402
and
Anthony N. Palazotto†
U.S. Air Force Institute of Technology, Wright–Patterson Air Force Base, Ohio 45433-6583

The symbolic manipulator Mathematica is used to implement a procedure combining the theory of elasticity, differential geometry, calculus of variations, and variational techniques to derive and solve a set of equations that approximates the nonlinear steady-state response of pressurized spinning toroidal shells. The nonlinearity is geometric and the torus is fiber reinforced along its major direction. The resulting set of nonlinear equations is solved for various values of the applied pressure, fiber content, and spinning speeds. Qualitative results are obtained and linear results are compared and contrasted to nonlinear results.

Introduction

TOROIDAL shells are important structural elements because of their closed shape that gives them enhanced rigidity. However, studies of toroidal shells are limited. Studies of the free vibrations of isotropic toroidal shells[1,2] show that these shells can perform two independent classes of axisymmetric free vibrations: motions that involve displacements along the major direction only, i.e., along θ_1 in Fig. 1; and motions that involve displacements along the minor and transverse directions only, i.e., along θ_2 and z in Fig. 1. Numerical solutions for prestressed toroidal membranes were presented by Liepins[3] for isotropic toroidal shells. The study used a linearized membrane theory and reported four families of modes. It concluded that only low-frequency modes that are predominantly flexural are strongly dependent on the prestress. Experimental studies of the vibrations of pressurized isotropic torus shells were reported by Jordan[4] and reproduced numerically by Liepins.[5] The numerical results simulated the free vibrations of prestressed isotropic toroidal membranes made of a number of toroidal segments each with a constant thickness. Li and Steigmann[6] studied finite deformations of toroidal membranes and showed that multiple equilibria are possible for rubberlike toroidal membranes.

The present research uses theory of elasticity and differential geometry to derive a set of nonlinear kinematic relationships and equations of motion for orthotropic toroidal shells. The nonlinearity is geometric and of the von Kármán type, i.e., only the transverse displacement contributes to the nonlinear strain-displacements relationships. The form of the assumed displacements satisfies the Love–Kirchhoff's assumptions, i.e., normal to the middle surface remains normal and its length does not change. The Lagrangian of the torus is assembled and two spatial dependencies are assumed allowing the explicit integration over their respective domains. All integrations were performed using a symbolic five-point Gaussian integration algorithm. Next, the equations of motion are derived by minimizing the Lagrangian, and the Galerkin procedure is used to reduce them to a set of nonlinear differential equations in the temporal domain. Assuming steady-state conditions and sufficient damping, the nonlinear differential equations of motion reduce to nonlinear algebraic equations for the amplitudes of the respective displacements. Numerical results show that tensile stresses are more sensitive to spinning speeds than compressive stresses. The model also predicts that the differences between linear and nonlinear in-plane stresses are larger in the case of internal pressure than in the case of external pressure. The model predicts that the torus would bulge under the combined action of applied pressure and centrifugal forces due to spinning. The algebraic manipulations and numerical solutions were performed using the symbolic manipulator Mathematica.[7]

Received Dec. 8, 1995; revision received July 10, 1996; accepted for publication Aug. 31, 1996; also published in *AIAA Journal on Disc*, Volume 2, Number 1. This paper is declared a work of the U.S. Government and is not subject to copyright protection in the United States.

*Associate Professor, Mechanical Engineering Department. Member AIAA.
†Professor, Department of Aeronautics and Astronautics. Associate Fellow AIAA.

Mathematical Formulation

Kinematics and Strain Energy

Figure 1 shows the geometry of a toroidal shell and the toroidal coordinate system $\{\theta_1, \theta_2, z\}$. The displacement fields along the

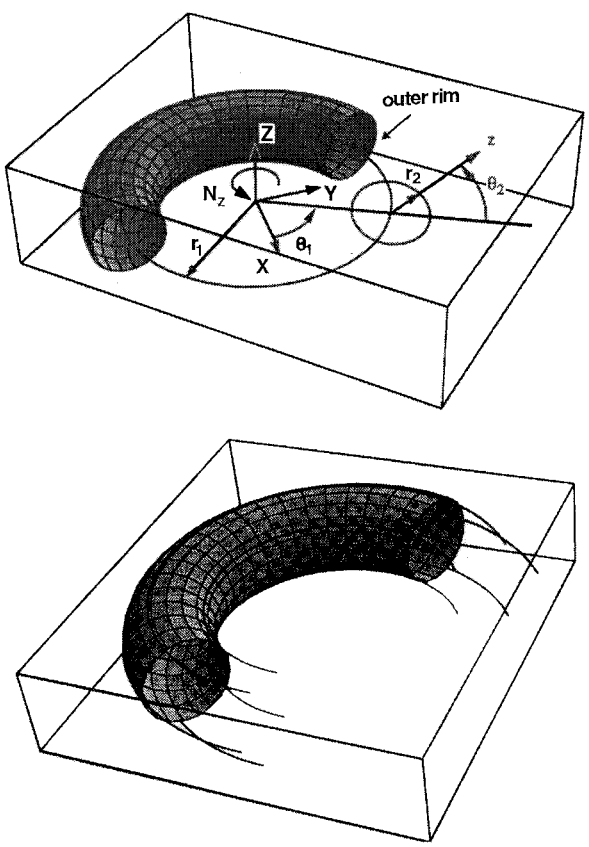

Fig. 1 Toroidal geometry and reinforcing scheme.

$\{\theta_1, \theta_2, z\}$ coordinate system are $u(\theta_1, \theta_2, z, t)$, $v(\theta_1, \theta_2, z, t)$, and $w(\theta_1, \theta_2, z, t)$, respectively, and the metric of the space is[8]

$$g_{11} = [r_1 + (r_2 + z)\cos\theta_2]^2 \qquad g_{22} = (r_2 + z)^2$$
$$g_{33} = 1 \qquad g_{ij} = 0 \qquad i \neq j \tag{1}$$

The metric of the space is diagonal because the chosen coordinate system is orthogonal. The strain-displacement relationships for a general orthogonal curvilinear coordinate system are given by[9]

$$\epsilon_{lm} = \epsilon^L_{lm} + \epsilon^N_{lm} \tag{2}$$

where

$$\epsilon^L_{lm} = \tfrac{1}{2}\left(g_{lk}v^k_{;m} + g_{km}v^k_{;l}\right) \qquad \epsilon^N_{lm} = \tfrac{1}{2}\left(g_{kr}v^k_{;l}v^r_{;m}\right) \tag{3}$$

where the superscript L denotes linear; the superscript N denotes nonlinear; v^k is the displacement vector; $v^l_{;n} = v^l_{,n} + \Gamma^l_{rn}v^r$, Γ^l_{rn} is the Christoffel symbol; and the $\{1, 2, 3\}$ indices refer to the $\{\theta_1, \theta_2, z\}$ coordinates, respectively. The expanded form of strain-displacement relationships is given explicitly by Raouf and Palazotto.[8]

The present paper considers a toroidal shell reinforced along its major direction, Fig. 1. The material is specially orthotropic and obeys a special form of Hooks law[10]

$$\begin{Bmatrix}\sigma_{11}\\ \sigma_{22}\\ \sigma_{12}\end{Bmatrix} = \begin{bmatrix}Q_{11} & Q_{12} & 0\\ Q_{12} & Q_{22} & 0\\ 0 & 0 & Q_{66}\end{bmatrix}\begin{Bmatrix}\epsilon_{11}\\ \epsilon_{22}\\ 2\epsilon_{12}\end{Bmatrix} \tag{4}$$

where Q_{ij} are elements of the stiffness matrix. Note that the constitutive law, Eq. (4), ignores out-of-plane stress. This is a consequence of the Love–Kirchhoff's assumptions. 1) Normal to the middle surface before deformation remains normal after deformation. This implies no transverse shear strain, i.e., $\epsilon_{13} = \epsilon_{23} = 0$. For orthotropic material, this also means zero transverse shear stresses. Accordingly, transverse shears are ignored in Eq. (4). 2) Normal to middle surface before deformation does not change its length after deformation. This implies that $\epsilon_{33} = 0$. Accordingly, the non-zero σ_{33} does not contribute to the strain energy of the system (its contribution is $\sigma_{33}\epsilon_{33} = 0$) and is ignored in Eq. (4).

The following displacement field satisfies the Love–Kirchhoff's assumptions in toroidal coordinates:

$$u(\theta_1, \theta_2, z, t) = U_0(\theta_1, \theta_2, t) + \frac{z}{r_1 + r_2\cos\theta_2} \times \left[U_0(\theta_1, \theta_2, t)\cos\theta_2 - W_{0,\theta_1}(\theta_1, \theta_2, t)\right]$$
$$v(\theta_1, \theta_2, z, t) = V_0(\theta_1, \theta_2, t) + (z/r_2)\left[V_0(\theta_1, \theta_2, t) + W_{0,\theta_2}(\theta_1, \theta_2, t)\right] \tag{5}$$
$$w(\theta_1, \theta_2, z, t) = W_0(\theta_1, \theta_2, t)$$

where the comma indicates differentiation with respect to the variable following it and U_0, V_0, and W_0 are the displacements of the middle surface in the $\{\theta_1, \theta_2, z\}$ directions, respectively. Following the Rayleigh–Ritz technique, the displacements of the middle surface are expanded in a set of admissible functions. In this study, these functions only have to satisfy the conditions of periodicity,

$$U_0(\theta_1, \theta_2, t) = \Sigma_n \eta_n(\theta_2, t)\sin n\theta_1$$
$$V_0(\theta_1, \theta_2, t) = \Sigma_n \chi_n(\theta_2, t)\cos n\theta_1 \tag{6}$$
$$W_0(\theta_1, \theta_2, t) = \Sigma_n \xi_n(\theta_2, t)\cos n\theta_1$$

We consider the case $n = 0$; this corresponds to the second class of motion identified in Refs. 1 and 2. This is consistent with the uniform loading considered in this paper and yields the following displacement field:

$$U_0(\theta_1, \theta_2, t) = 0 \qquad V_0(\theta_1, \theta_2, t) = \chi_0(\theta_2, t)$$
$$W_0(\theta_1, \theta_2, t) = \xi_0(\theta_2, t) \tag{7}$$

and the corresponding strain-displacement relationships are

$$\epsilon^{\mathcal{L}}_{11} = \frac{\cos(\theta_2)\,\xi_0 - \sin(\theta_2)\left[\chi_0 + (z\chi_0/r_2) - \left(z\xi_{0,\theta_2}/r_2\right)\right]}{r_1 + r_2\cos(\theta_2) + z\cos(\theta_2)}$$
$$\epsilon^{\mathcal{L}}_{22} = \frac{1}{r_2 + z}\left(\xi_0 + \chi_{0,\theta_2} + \frac{z\chi_{0,\theta_2}}{r_2} - \frac{z\xi_{0,\theta_2\theta_2}}{r_2}\right)$$
$$\epsilon^{\mathcal{N}}_{11} = \frac{\left\{\cos(\theta_2)\xi_0(\theta_2, t) - \sin(\theta_2)\left[\chi_0 + (z\chi_0/r_2) - \left(z\xi_{0,\theta_2}/r_2\right)\right]\right\}^2}{2[r_1 + r_2\cos(\theta_2) + z\cos(\theta_2)]^2} \tag{8}$$
$$\epsilon^{\mathcal{N}}_{22} = \left[\frac{(r_2 + z)^2\left(-\chi_0 + \xi_{0,\theta_2}\right)^2}{r_2^2} + \left(\xi_0 + \chi_{0,\theta_2} + \frac{z\chi_{0,\theta_2}}{r_2} - \frac{z\xi_{0,\theta_2\theta_2}}{r_2}\right)^2\right] \Big/ 2(r_2 + z)^2$$

and

$$\epsilon^{\mathcal{L}}_{12} = \epsilon^{\mathcal{N}}_{12} = 0 \qquad \epsilon^{\mathcal{L}}_{31} = \epsilon^{\mathcal{N}}_{31} = 0 \qquad \epsilon^{\mathcal{L}}_{32} = 0 \tag{9}$$

Note that $\epsilon^{\mathcal{N}}_{32}$ is not zero; however, it is a higher-order strain expansion and will be ignored in this study. The strain energy of the torus Π is

$$\Pi = \frac{1}{2}\int (\epsilon_{11}\sigma_{11} + \epsilon_{22}\sigma_{22})\sqrt{g_{11}g_{22}g_{33}}\,\mathrm{d}\theta_1\,\mathrm{d}\theta_2\,\mathrm{d}z \tag{10}$$

Kinetic Energy and Equations of Motion

The deformed position vector of a point in the body of the torus is given by

$$\boldsymbol{r} = \cos\theta_1[r_1 + (r_2 + z)\cos\theta_2]\,\boldsymbol{i} + \{\sin\theta_1[r_1 + (r_2 + z)\cos\theta_2]\}\,\boldsymbol{j} + (r_2 + z)\sin\theta_2\boldsymbol{k} + u\boldsymbol{e}_{\theta_1} + v\boldsymbol{e}_{\theta_2} + w\boldsymbol{e}_z \tag{11}$$

where $\boldsymbol{i}, \boldsymbol{j}$, and $\boldsymbol{k}$ are unit vectors along the X, Y, and Z directions and $\boldsymbol{e}_{\theta_1}$, $\boldsymbol{e}_{\theta_2}$, and $\boldsymbol{e}_z$ are unit vectors in the θ_1, θ_2, and z directions (Fig. 1). These unit vectors are given by

$$\boldsymbol{e}_{\theta_1} = \frac{1}{\sqrt{g_{11}}}\frac{\partial \boldsymbol{r}}{\partial\theta_1} = -\sin\theta_1\boldsymbol{i} + \cos\theta_1\,\boldsymbol{j}$$
$$\boldsymbol{e}_{\theta_2} = \frac{1}{\sqrt{g_{22}}}\frac{\partial \boldsymbol{r}}{\partial\theta_2} = -\sin\theta_2\cos\theta_1\boldsymbol{i} - \sin\theta_2\sin\theta_1\,\boldsymbol{j} + \cos\theta_2\boldsymbol{k} \tag{12}$$
$$\boldsymbol{e}_z = \frac{1}{\sqrt{g_{33}}}\frac{\partial \boldsymbol{r}}{\partial z} = -\cos\theta_2\cos\theta_1\boldsymbol{i} - \cos\theta_2\sin\theta_1\,\boldsymbol{j} + \sin\theta_2\boldsymbol{k}$$

The velocity vector of a point in the body of the torus is given by the transport theorem[11]

$$\boldsymbol{v} = \frac{\mathrm{d}\boldsymbol{r}}{\mathrm{d}t} + \boldsymbol{\Omega}\times\boldsymbol{r} \tag{13}$$

where $\boldsymbol{\Omega}$ is the spin vector, which represents rigid body rotations of the torus. In the present study, the torus is spinning around the Z axis with an angular speed N_z. Accordingly,

$$\boldsymbol{\Omega} = N_z\boldsymbol{k} \tag{14}$$

and the kinetic energy of the torus is thus

$$K = \int \frac{1}{2}\rho|\boldsymbol{v}|^2\sqrt{g_{11}g_{22}g_{33}}\,\mathrm{d}\theta_1\,\mathrm{d}\theta_2\,\mathrm{d}z \tag{15}$$

where ρ is the mass density and $|\boldsymbol{v}|$ is the magnitude of the velocity of a point in the body of the torus.

Assuming small elastic rotations, the work done by the applied pressure is conservative and independent of θ_1. It is given by the applied pressure P times the displaced volume and can be expressed as[12]

$$W = -Pr_2\int\left[w + \frac{1}{2r_2}\left(v^2 - vw_{,\theta_2} + v_{,\theta_2}w + w^2\right)\right] \times \sqrt{g_{11}g_{22}}\,\mathrm{d}\theta_1\,\mathrm{d}\theta_2 \tag{16}$$

The pressure is assumed to act on the middle surface, and displacements are evaluated at $z = 0$ (middle surface). The Lagrangian is given by

$$L = K - \Pi - W \tag{17}$$

Applying Hamilton's principle, the equations of equilibrium are derived using the Euler–Lagrange equations

$$\frac{\partial L}{\partial q_i} - \frac{\partial}{\partial \theta_2}\frac{\partial L}{\partial (q_{i,\theta_2})} - \frac{\partial}{\partial t}\frac{\partial L}{\partial (q_{i,t})} + \frac{\partial^2}{\partial \theta_2^2}\frac{\partial L}{\partial (q_{i,\theta_2\theta_2})} = 0 \tag{18}$$

where $q_i = \{\xi_0(\theta_2, t), \chi_0(\theta_2, t)\}$. Equations (18) are nonlinear partial differential equations. A solution to these equations can be approximated using the Galerkin procedure and the following assumed mode shapes:

$$\begin{aligned} \chi_0(\theta_2, t) &= \chi_1(t) + \chi_s(t)\sin\theta_2 + \chi_c(t)\cos\theta_2 \\ \xi_0(\theta_2, t) &= \xi_1(t) + \xi_s(t)\sin\theta_2 + \xi_c(t)\cos\theta_2 \end{aligned} \tag{19}$$

The assumed θ_2 dependencies have to satisfy only the periodicity conditions. Equations (19) represent the leading terms in the expansion of χ_0 and ξ_0. Higher modes and their coupling effects are ignored. Following the Galerkin procedure,[13] Eqs. (18) reduce to a set of six nonlinear temporal differential equations in $\xi_1(t)$, $\xi_s(t)$, $\xi_c(t)$, $\chi_1(t)$, $\chi_s(t)$, and $\chi_c(t)$ of the form

$$[M]\{\ddot{x}\} + [K]\{x\} + \{q(x)\} = \{f\} \tag{20}$$

where $\{x\}^T = \{\chi_1(t), \chi_s(t), \chi_c(t), \xi_1(t), \xi_s(t), \xi_c(t)\}$ and $\{q(x)\}$ is a cubic nonlinear function in $\chi_1(t)$, $\chi_s(t)$, and $\chi_c(t)$. For the example presented in the Numerical Results section, Eq. (20) yields

$[M]$ = mass matrix

$$= \begin{bmatrix} 631.6 & 0 & 256.9 & 0 & 0 & 0 \\ 0 & 349.0 & 0 & 0 & 0 & 0 \\ 256.9 & 0 & 282.7 & 0 & 0 & 0 \\ 0 & 0 & 0 & 631.6 & 0 & 256.9 \\ 0 & 0 & 0 & 0 & 349.0 & 0 \\ 0 & 0 & 0 & 256.9 & 0 & 282.7 \end{bmatrix} \tag{21}$$

$$\{f\} = \text{force vector} = \begin{Bmatrix} 0 \\ -7950.8N_z^z \\ 0 \\ 9659.9N_z^2 - 10106.2P \\ 0 \\ 8791.6N_z^2 - 4109.7P \end{Bmatrix} \tag{22}$$

Here, $k_{ij} = k_{ij}(P, N_z^2)$ is the linear stiffness matrix and q_i is a nonlinear vector. Both are listed explicitly in the Appendix. Assuming steady-state conditions and viscous damping, the temporal dependency is dropped, i.e., $\mathrm{d}(\ )/\mathrm{d}t = 0$, and the equations of motion are reduced to nonlinear algebraic equations. The following section is devoted to studying the solutions of these equations. The nonlinear algebraic equations are solved numerically using the built in Newton–Raphson algorithm in Mathematica.[7]

Numerical Results

This section presents numerical studies of a spinning composite torus made of rubber and reinforced with nylon fibers along its major direction as shown in Fig. 1. The elastic properties of the constituents are given in Table 1. The effective properties of the laminated construction are obtained using the Halpin–Tsai technique.[10] A fiber volume fraction of 0.6 is used, except in Fig. 4. The torus

Table 1 Properties of constituent materials

Elastic constant	Nylon fiber	Rubber matrix
E	281 ksi	800 psi
G	70.55 ksi	268 psi
ν_{12}	0.9915	0.49

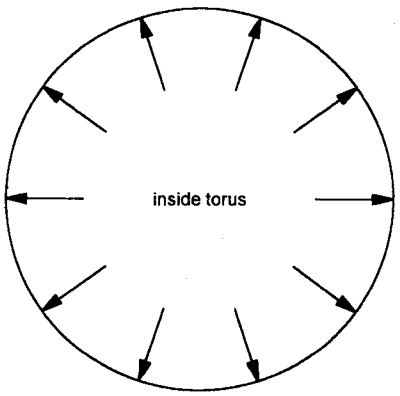

Fig. 2 Section in an undeformed torus, at θ_1 = constant, under internal pressure.

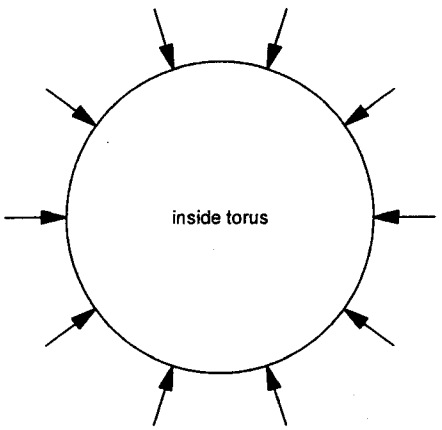

Fig. 3 Section in an undeformed torus, at θ_1 = constant, under external pressure.

has a major radius $r_1 = 20$ in., a minor radius $r_2 = 16$ in., and a thickness $h = 0.05$ in. Two loading cases are considered. The first is internal pressure. This pressure is uniformly distributed on the inner surface of the torus and acts along the positive z axis (Fig. 2). This loading induces mainly tensile stresses within the body of the torus. An example of this loading is the inflation pressure in a tire.

The second is external pressure. This pressure is uniformly distributed on the outer surface of the torus and acts along the negative z axis, Fig. 3. This loading induces mainly compressive stresses within the body of the torus. An example of this loading is fluid loading on a submerged torus.

The present analysis can be reduced to the case considered by Timoshenko and Woinowsky-Krieger[14] for stationary isotropic tori under a uniform dead load. It predicts stresses to within 25%. This can be attributed to the fact that the present formulation contains bending action whereas Timoshenko and Woinowsky-Krieger[14] ignore bending.

Figure 4 shows the steady-state amplitudes as a function of the fiber volume fraction for an externally loaded torus. Note that the uniform loading does not excite all of the assumed modes in Eq. (19). In particular, the loading excites the even (cosinosoidal) harmonics of the transverse displacement w and the odd (sinusoidal) harmonics of the in-plane displacement v. Figure 4 shows that the discrepancies between the linear and nonlinear solution decrease as the fiber volume fraction increases and the torus becomes stiffer. Moreover, the nonlinearities are more pronounced in the transverse deflection components ξ_1 and ξ_c. This is a result of the von Kármán assumptions.

The remainder of this section is devoted to studying the in-plane stress fields in the torus. In all of the studied cases, and for any given θ_2, the in-plane stresses are almost constant across the thickness. Accordingly, no through the thickness variations are reported except to explain specific phenomena.

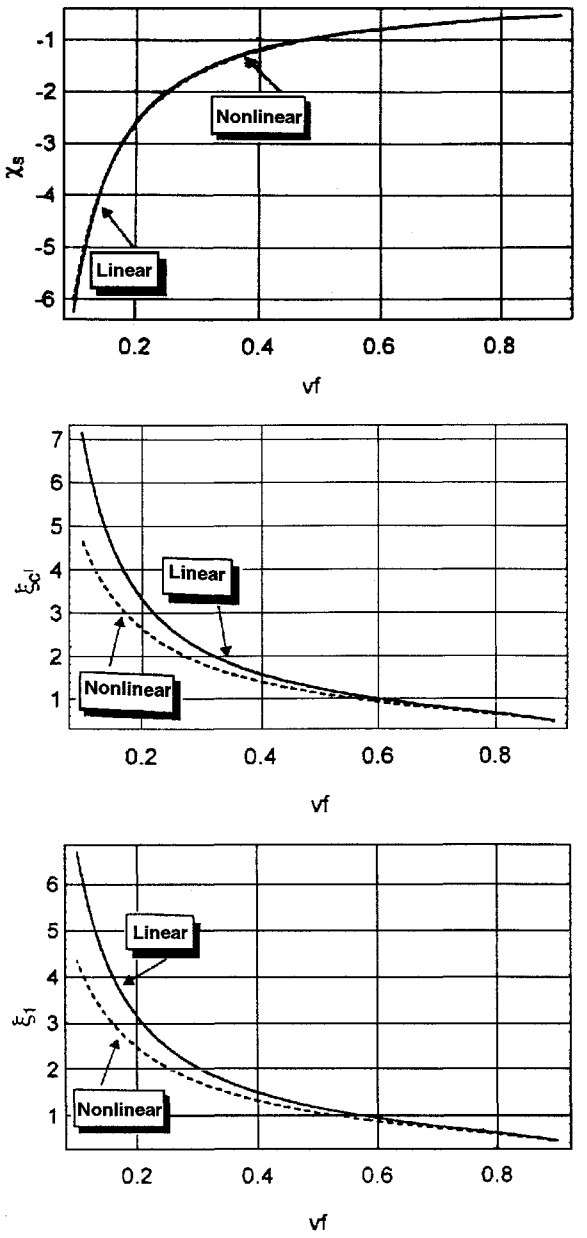

Fig. 4 Steady-state amplitudes of the response of an externally loaded torus as a function of fiber volume fraction: ξ_1 and ξ_c are components of the transverse deflection, and χ_s is a component of the in-plane deflection along the θ_2 direction; all other deflection components are zero.

Figures 5 and 6 show the distribution of the in-plane stresses as a function of θ_2 for a torus under an internal pressure of 5 psi and spinning at 100 and 500 rad/s, respectively. The torus experiences tensile stresses at its outer rim, i.e., around $\theta_2 = 0, 2\pi$, and compressive stresses at its inner rim, i.e., around $\theta_2 = \pi$. This is due to centrifugal forces that reinforce the internal pressure at the outer rim and opposes it at the inner rim. Linear analysis predicts a significant increase in tensile stresses as the spinning speed increases, from a maximum of about 80 ksi at 100 rad/s to about 130 ksi at 500 rad/s. However, nonlinear analysis predicts a much smaller increase, from a maximum of about 50 ksi at 100 rad/s to about 60 ksi at 500 rad/s.

On the other hand, increasing the spinning speed does not have a significant effect on the compressive stresses at the inner rim. Figures 5 and 6 also show significant discrepancies between the linear and nonlinear stress fields for both cases with the linear stress being usually higher in magnitude. Moreover, the nonlinear stress field is more uniform and assumes less fluctuation than the linear stress field.

Figure 7 shows the deformation of a section in an internally loaded torus at any θ_1 due to 5-psi pressure and 500-rad/s spinning speed. The linear solution predicts larger deformations than

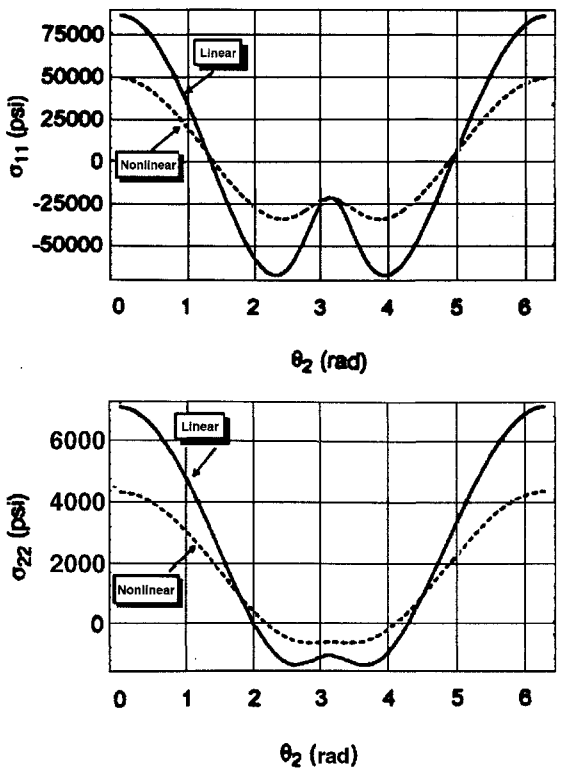

Fig. 5 Distribution of the in-plane stresses as a function of θ_2 for an internal pressure of 5 psi and a spinning speed of 100 rad/s.

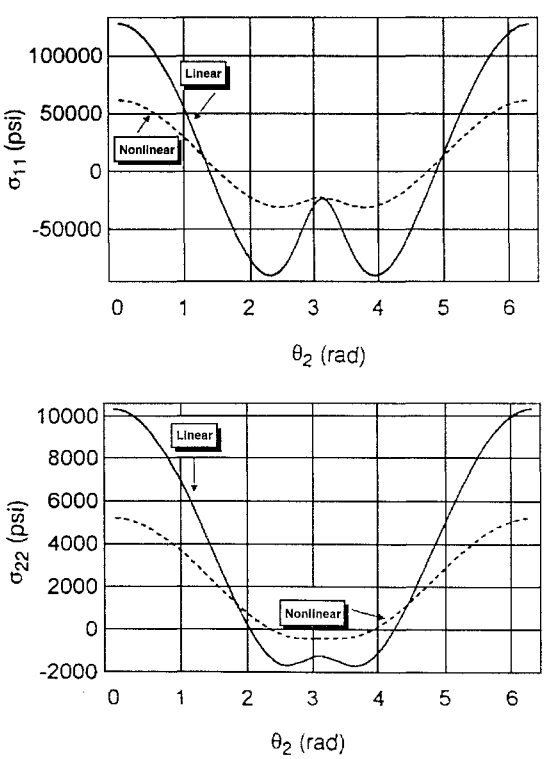

Fig. 6 Distribution of the in-plane stresses as a function of θ_2 for an internal pressure of 5 psi and a spinning speed of 500 rad/s.

the nonlinear solution. This is consistent with the predicted stress fields in Fig. 6. Moreover, Fig. 7 shows a slight bulging at the inner rim. To fully explain the bulging at the inner rim, Fig. 8 shows details of the in-plane stress fields around the inner rim, i.e., $\theta_2 = \pi$. Figure 8 depicts in-plane stresses at the inner and outer surfaces of the torus. It shows that the torus is in compression at that region and that the stresses are almost constant with the stresses on the outer surface being slightly greater than the stresses on the

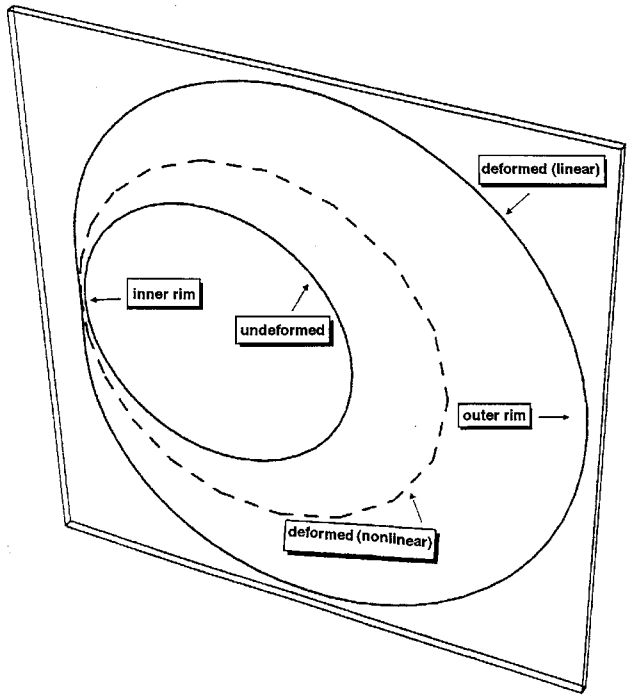

Fig. 7 Section in torus showing deformed and undeformed shapes due to 5-psi internal pressure and 500-rad/s spinning speed. Notice the slight bulging at the left side of the deformed linear shape.

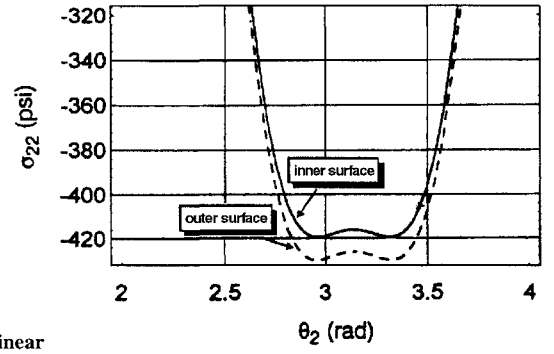

Nonlinear

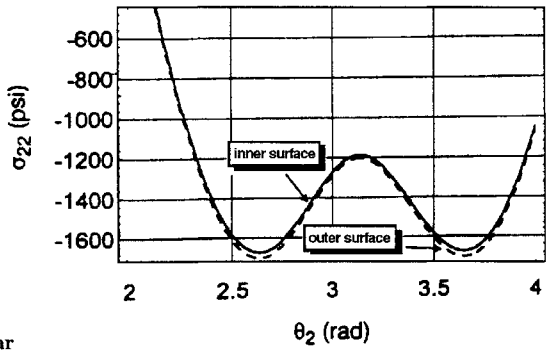

Linear

Fig. 8 In-plane stress distribution as a function of θ_2 around the inner rim for a torus under an internal pressure of 5 psi at 500 rad/s.

inner surface giving rise to the stress distribution shown in Fig. 9. This stress distribution can be decomposed into a constant compressive stress (equal to average of stresses at the inner and outer surfaces of the torus) and linear stress distribution, which produces the shown resultant bending moment and hence the bulged shape. Strength of materials arguments show that the bending moment is proportional to the difference between the surface stress and the average stress. Figure 10 shows the difference between the surface and average stress as a function of θ_2. A higher value indicates a higher bending moment and accordingly larger bulging. Figure 10

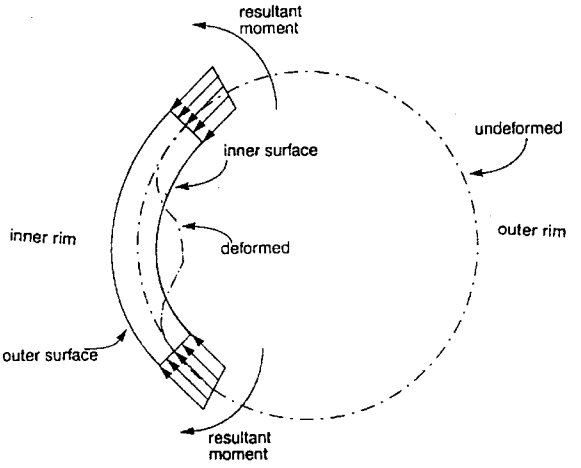

Fig. 9 Section in the torus at a constant θ_1; only quantities around the inner rim are shown.

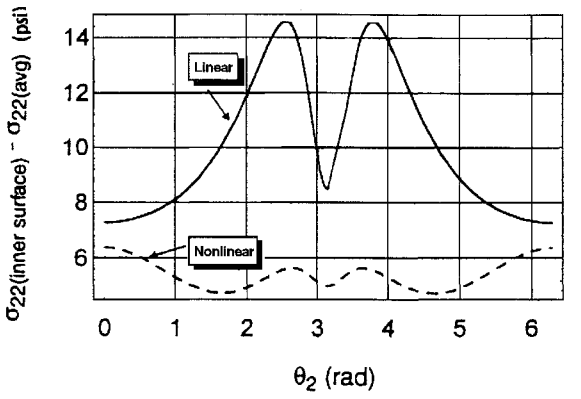

Fig. 10 Difference between the average and surface compressive stress for a torus under a 5-psi internal pressure spinning at 500-rad/s.

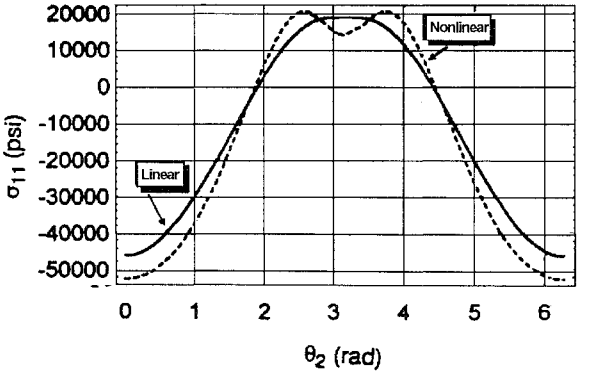

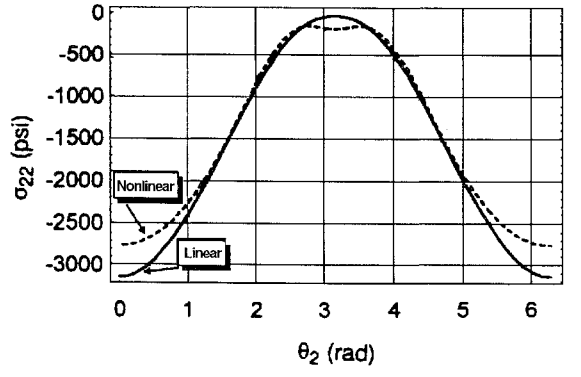

Fig. 11 Distribution of the in-plane stresses as a function of θ_2 in a stationary torus under an external pressure of 10 psi.

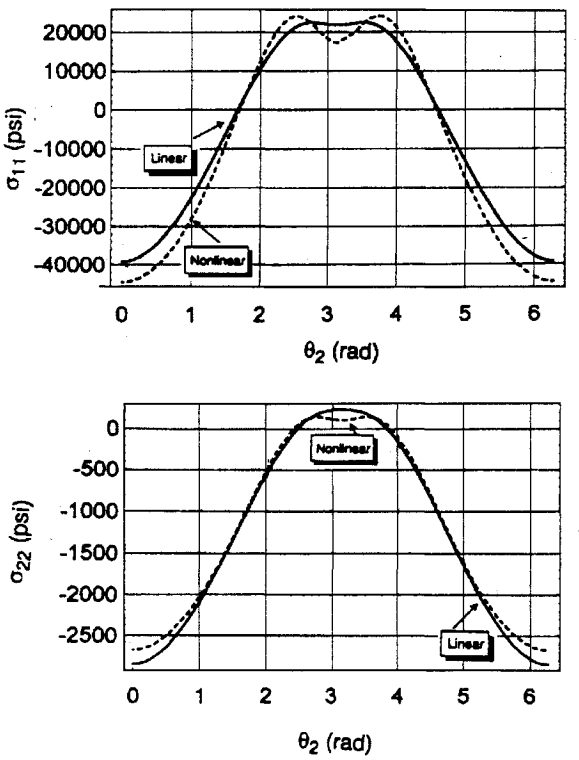

Fig. 12 Distribution of the in-plane stresses as a function of θ_2 for an external pressure of 10 psi and a spinning speed of 500 rad/s.

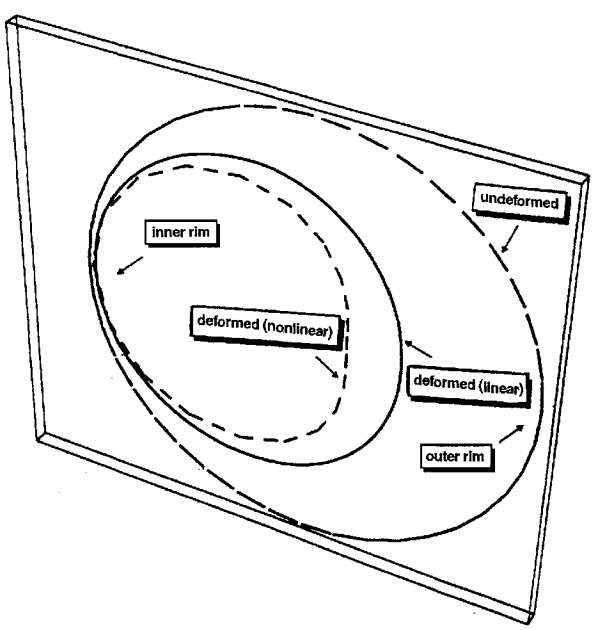

Fig. 13 Section in torus showing deformed and undeformed shapes due to 10-psi external pressure and 1-rad/s spinning speed. Notice the slight bulging at the right side of the deformed nonlinear shape.

shows that the linear solution produces a higher bending moment than the nonlinear solution. This explains why the linear solution in Fig. 7 shows more bulging.

Next, the torus is studied under compressive, external load. Figures 11–15 study the in-plane stress distributions for a torus with volume fraction $v_f = 0.6$ and under an external load of 10 psi. Note that the externally loaded torus required a higher pressure but slower spinning speed to exhibit similar characteristics as the internally loaded torus. Figures 11 and 12 show the in-plane stress distribution for a stationary torus and torus spinning at 500 rad/s under an external load of 10 psi. Figures 11 and 12 both show that the torus is

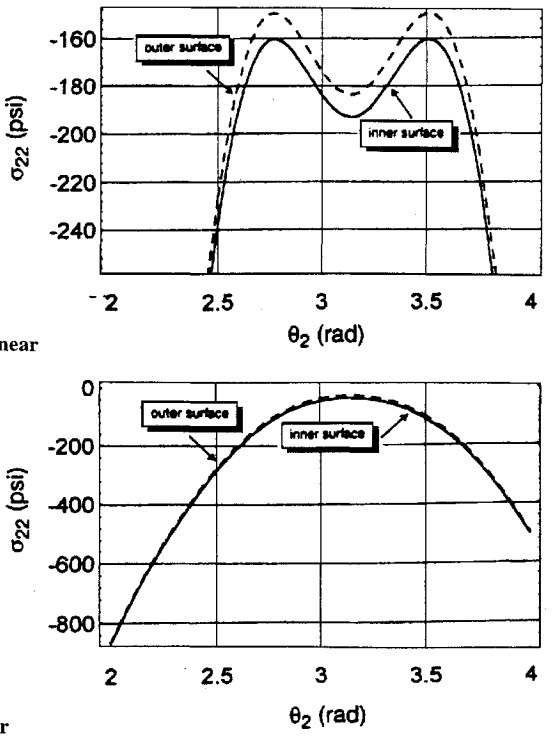

Fig. 14 In-plane stress distribution as a function of θ_2 around the inner rim for a torus under an external pressure of 10 psi at 1 rad/s.

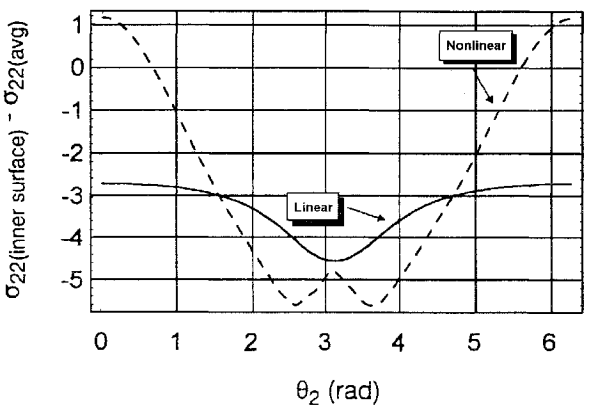

Fig. 15 Difference between the average and surface compressive stress for a torus under a 10-psi external pressure spinning at 1 rad/s.

mainly in compression and, unlike the internal pressure cases shown in Figs. 5 and 6, there is no significant difference between the linear and nonlinear solutions. However, similar to the case of internal pressure, the effects of spinning on compressive stresses are small. Another similarity between the internal and external pressure cases is the fact that the stress field at the outer and inner rims have opposite sign stresses. This is not true for σ_{22} in a stationary torus under external pressure. This is supported by an examination of the deformed shape in Fig. 13, which shows that bulging occurs at the outer rim of the torus. Moreover, more bulging is predicted by the nonlinear solution than by the linear solution. A closer examination of the stress fields around the inner rim is shown in Fig. 14. It shows that the stress at the inner rim is compressive; however, the stress at the outer surface is higher, as before, than the stress at the inner surface. A study of the resulting bending moment confirms that bulging occurs at the outer rim of the torus. Last, Fig. 15 shows the difference between the average stress and the surface stress. As explained in the case of internal pressure, this is a measure of the magnitude of the resultant bending moment. Figure 15 shows that the nonlinear analysis produces a wider variation of stress, resulting in a higher bending moment. Accordingly, bulging is more pronounced in the nonlinear solution.

Conclusions

The nonlinear equations of motion that describe the response of a spinning orthotropic toroidal shell are derived, and a qualitative analysis of the response of the torus is conducted. The mathematical model is based on the theory of elasticity and calculus of variations. Numerical experimentations are conducted to study the in-plane stress fields in the torus under internal and external pressures. Results show that the linear and nonlinear stress fields differ considerably for the case of internal pressure but are very close in the case of external pressure. Moreover, tensile stresses are more sensitive to spinning speed than compressive stresses. The model also predicts bulging in the torus as a result of the combined action of centrifugal and applied loads. Internal pressure cases show that the nonlinearity offers more resistance to bending deformations and bulging occurs in the linear solution. On the other hand, external pressure cases show that the nonlinearity offers less resistance to bending deformations and shows the bulging behavior.

Appendix: Explicit Terms in Eq. (20)

The elements of the stiffness matrix in Eq. (20) are

$$k_{21} = k_{41} = k_{61} = k_{12} = k_{32} = k_{52} = k_{23} = k_{43} = k_{63} = 0$$

$$k_{14} = k_{34} = k_{54} = k_{25} = k_{45} = k_{65} = k_{16} = k_{36} = k_{56} = 0$$

$$k_{11} = -348.967N_z^2 + 631.64065P + 1.39439Q_{11}$$

$$k_{31} = -60.7189N_z^2 + 256.85526P + 0.19802Q_{11} + 1.00341Q_{12}$$

$$k_{51} = 60.71915N_z^2 - 124.226P - 0.19801Q_{11} - 0.97051Q_{12}$$

$$k_{22} = -323.803N_z^2 + 348.96672P + 1.34190Q_{11} + 0.15001Q_{12} + 3.02631Q_{22}$$

$$k_{42} = 60.71904N_z^2 + 132.62922P - 0.198019Q_{11} + 0.03290Q_{12} + 2.00667Q_{22}$$

$$k_{62} = 25.16323N_z^2 + 263.47232P - 0.05249Q_{11} - 0.30008Q_{12} + 2.20838Q_{22}$$

$$k_{13} = -60.71890N_z^2 + 256.85526P + 0.19802Q_{11} + 1.00341Q_{12} + 0.06565Q_{22}$$

$$k_{33} = -25.16335N_z^2 + 282.67393P + 0.05249Q_{11} - 0.150Q_{12} + 1.90836Q_{22}$$

$$k_{53} = 25.16383N_z^2 - 368.168P - 0.05249Q_{11} - 0.30002Q_{12} - 2.7263Q_{22}$$

$$k_{24} = 60.71880N_z^2 + 124.22544P - 0.19802Q_{11} + 1.94101Q_{22}$$

$$k_{44} = -282.673N_z^2 + 631.63911P + 4.89992Q_{11} - 0.00012Q_{12} + 4.93468Q_{22}$$

$$k_{64} = -196.135N_z^2 + 256.85443P - 4.11807Q_{11} + 2.00682Q_{12} + 2.00667Q_{22}$$

$$k_{15} = 60.71890N_z^2 - 132.63P - 0.19802Q_{11} - 1.00341Q_{12} - 0.06565Q_{22}$$

$$k_{35} = 25.16335N_z^2 - 263.472P - 0.05249Q_{11} + 0.15007Q_{12} - 1.90836Q_{22}$$

$$k_{55} = -25.1638N_z^2 + 348.96691P + 0.05249Q_{11} + 0.30002Q_{12} + 2.72629Q_{22}$$

$$k_{26} = 25.16275N_z^2 + 368.16823P - 0.05249Q_{11} + 0.15001Q_{12} + 3.02631Q_{22}$$

$$k_{46} = -196.135N_z^2 + 256.85446P - 4.11807Q_{11} + 2.00682Q_{12} + 2.00667Q_{22}$$

$$k_{66} = -257.51N_z^2 + 282.67374P + 4.84743Q_{11} - 0.30015Q_{12} + 2.20838Q_{22}$$

The elements of the nonlinear vector $\{q\}$ in Eq. (20) are

$$q_1 = -0.02812Q_{12}\xi_c\xi_s + 0.01875Q_{22}\xi_c\xi_s - 0.18197Q_{12}\xi_s\xi_1 + 0.12131Q_{22}\xi_s\xi_1 - 0.02813Q_{12}\xi_c\chi_c + 0.01875Q_{22}\xi_c\chi_c - 0.05860Q_{12}\xi_1\chi_c + 0.12131Q_{22}\xi_1\chi_c + 0.02812Q_{12}\xi_s\chi_s - 0.01875Q_{22}\xi_s\chi_s - 0.00100Q_{11}\chi_c\chi_s - 0.12830Q_{12}\chi_c\chi_s + 0.12542Q_{22}\xi_c\chi_1 - 3.80022\times10^{-6}Q_{12}\xi_1\chi_1 + 0.30842Q_{22}\xi_1\chi_1 - 0.00183Q_{11}\chi_s\chi_1 + 0.01678Q_{12}\chi_s\chi_1 - 0.12952Q_{22}\chi_s\chi_1 + 0.03279Q_{22}\chi_c\chi_s + 0.06271Q_{12}\xi_c\chi_1$$

$$q_2 = -0.00466Q_{12}\xi_c^2 + 0.00310Q_{22}\xi_c^2 - 0.08633Q_{12}\xi_s^2 + 0.05755Q_{22}\xi_s^2 - 0.02812Q_{12}\xi_c\xi_1 + 0.01875Q_{22}\xi_c\xi_1 - 0.09098Q_{12}\xi_1^2 + 0.06065Q_{22}\xi_1^2 - 0.11200Q_{12}\xi_s\chi_c + 0.11510Q_{22}\xi_s\chi_c - 0.00043Q_{11}\chi_c^2 - 0.02533Q_{12}\chi_c^2 + 0.09030Q_{22}\chi_c^2 + 0.00931Q_{12}\xi_c\chi_s - 0.00621Q_{22}\xi_c\chi_s + 0.02813Q_{12}\xi_1\chi_s - 0.01875Q_{22}\xi_1\chi_s - 0.00048Q_{11}\chi_s^2 - 0.02959Q_{12}\chi_s^2 + 0.03101Q_{22}\chi_s^2 + 0.00938Q_{12}\xi_s\chi_1 + 0.17039Q_{22}\xi_s\chi_1 - 0.00100Q_{11}\chi_c\chi_1 + 0.00442Q_{12}\chi_c\chi_1 + 0.35954Q_{22}\chi_c\chi_1 - 0.00091Q_{11}\chi_1^2 - 0.02460Q_{12}\chi_1^2 + 0.06066Q_{22}\chi_1^2$$

$$q_3 = -0.00931Q_{12}\xi_c\xi_s + 0.00621Q_{22}\xi_c\xi_s - 0.02813Q_{12}\xi_s\xi_1 - 0.02813Q_{12}\xi_1\chi_c + 0.01875Q_{22}\xi_1\chi_c + 0.00931Q_{12}\xi_s\chi_s - 0.00621Q_{22}\xi_s\chi_s - 0.00086Q_{11}\chi_c\chi_s + 0.07597Q_{12}\chi_c\chi_s - 0.06612Q_{22}\chi_c\chi_s - 0.00938Q_{12}\xi_c\chi_1 + 0.13802Q_{22}\xi_c\chi_1 + 0.06271Q_{12}\xi_1\chi_1 + 0.12542Q_{22}\xi_1\chi_1 - 0.00100Q_{11}\chi_s\chi_1 - 0.14870Q_{12}\chi_s\chi_1 - 0.25730Q_{22}\chi_s\chi_1 + 0.00621Q_{22}\xi_c\chi_c + 0.01875Q_{22}\xi_s\xi_1 + 0.05340Q_{12}\xi_c\chi_c$$

$$q_4 = 0.02344Q_{12}\xi_c^2 + 0.12013Q_{22}\xi_c^2 - 0.02343Q_{12}\xi_s^2 + 1.90011\times10^{-6}Q_{12}\xi_1^2 + 0.15420Q_{22}\xi_1^2 - 0.00099Q_{11}\xi_s\chi_c + 0.09522Q_{12}\xi_s\chi_c + 0.20617Q_{22}\xi_s\chi_c - 1.67004Q_{11}\chi_c^2 + 0.18971Q_{12}\chi_c^2 + 0.24111Q_{22}\chi_c^2 - 0.00099Q_{11}\xi_c\chi_s - 0.05789Q_{12}\xi_c\chi_s - 0.41065Q_{22}\xi_c\chi_s - 0.00182Q_{11}\xi_1\chi_s$$

$$
\begin{aligned}
&- 0.11925Q_{12}\xi_1\chi_s - 0.12131Q_{22}\xi_1\chi_s + 0.00149Q_{11}\chi_s^2 \\
&+ 0.03996Q_{12}\chi_s^2 + 0.37572Q_{22}\chi_s^2 - 0.00182Q_{11}\xi_s\chi_1 \\
&- 0.18729Q_{12}\xi_s\chi_1 + 0.12952Q_{22}\xi_s\chi_1 + 3.39919Q_{11}\chi_c\chi_1 \\
&- 0.19587Q_{12}\chi_c\chi_1 + 0.38035Q_{22}\chi_c\chi_1 - 1.66855Q_{11}\chi_1^2 \\
&+ 0.22968Q_{12}\chi_1^2 + 0.46262Q_{22}\chi_1^2 + 0.12131Q_{22}\xi_c\xi_1 \\
&+ 0.03407Q_{22}\xi_s^2 + 0.05860Q_{12}\xi_c\xi_1
\end{aligned}
$$

$$
\begin{aligned}
q_5 = {} & 0.10579Q_{12}\xi_c\xi_s + 0.01995Q_{22}\xi_c\xi_s - 0.02812Q_{12}\xi_s\xi_1 \\
&- 0.01875Q_{22}\xi_s\xi_1 - 0.00086Q_{11}\xi_c\chi_c + 0.04097Q_{12}\xi_c\chi_c \\
&- 0.00969Q_{22}\xi_c\chi_c - 0.00099Q_{11}\xi_1\chi_c - 0.03750Q_{12}\xi_1\chi_c \\
&- 0.01875Q_{22}\xi_1\chi_c - 0.00096Q_{11}\xi_s\chi_s - 0.16229Q_{12}\xi_s\chi_s \\
&+ 0.00969Q_{22}\xi_s\chi_s + 0.00258Q_{11}\chi_c\chi_s - 0.03266Q_{12}\chi_c\chi_s \\
&+ 0.06899Q_{22}\chi_c\chi_s - 0.00099Q_{11}\xi_c\chi_1 - 0.02976Q_{12}\xi_c\chi_1 \\
&- 0.35953Q_{22}\xi_c\chi_1 - 0.00182Q_{11}\xi_1\chi_1 - 0.12131Q_{12}\xi_1\chi_1 \\
&- 0.12131Q_{22}\xi_1\chi_1 + 0.00298Q_{11}\chi_s\chi_1 + 0.05180Q_{12}\chi_s\chi_1 \\
&+ 0.70032Q_{22}\chi_s\chi_1
\end{aligned}
$$

$$
\begin{aligned}
q_6 = {} & -0.02359Q_{12}\xi_c^2 - 0.01202Q_{22}\xi_c^2 - 0.00776Q_{12}\xi_s^2 \\
&- 0.03135Q_{12}\xi_1^2 + 0.06270Q_{22}\xi_1^2 - 0.00086Q_{11}\xi_s\chi_c \\
&- 0.08565Q_{12}\xi_s\chi_c + 0.24524Q_{22}\xi_s\chi_c + 1.69830Q_{11}\chi_c^2 \\
&- 0.05025Q_{12}\chi_c^2 + 0.21839Q_{22}\chi_c^2 - 0.00086Q_{11}\xi_c\chi_s \\
&+ 0.04303Q_{12}\xi_c\chi_s - 0.00559Q_{22}\xi_c\chi_s - 0.00099Q_{11}\xi_1\chi_s \\
&- 0.03750Q_{12}\xi_1\chi_s - 0.01875Q_{22}\xi_1\chi_s + 0.00129Q_{11}\chi_s^2 \\
&- 0.01735Q_{12}\chi_s^2 + 0.03244Q_{22}\chi_s^2 - 0.00099Q_{11}\xi_s\chi_1 \\
&+ 0.12335Q_{12}\xi_s\chi_1 + 0.25729Q_{22}\xi_s\chi_1 - 3.34008Q_{11}\chi_c\chi_1 \\
&- 0.09896Q_{12}\chi_1^2 + 0.18812Q_{22}\chi_1^2 + 0.01875Q_{22}\xi_c\xi_1 \\
&+ 1.69960Q_{11}\chi_1^2 + 0.40755Q_{12}\chi_c\chi_1 + 0.53334Q_{22}\chi_c\chi_1 \\
&+ 0.07473Q_{22}\xi_s^2 + 0.02813Q_{12}\xi_c\xi_1
\end{aligned}
$$

Acknowledgments

The authors acknowledge the support of Arje Nachman from the U.S. Air Force Office of Scientific Research and Arnold Mayer from the Vehicle Subsystems Division, Flight Dynamics Directorate, U.S. Air Force Wright Laboratories.

References

[1]McGill, D. J., "Axisymmetric Free Oscillations of Thick Toroidal Shells," Ph.D. Dissertation, Dept. of Mechanics and Aerospace Engineering, Univ. of Kansas, Lawrence, KS, June 1996.

[2]McGill, D. J., and Lenzen, K. H., "Polar Axisymmetric Free Oscillations of Thick Hollowed Tori," *SIAM Journal of Applied Mathematics*, Vol. 15, No. 3, 1967, pp. 678–692.

[3]Liepins, A. A., "Free Vibrations of Prestressed Toroidal Membrane," *AIAA Journal*, Vol. 3, No. 10, 1965, pp. 1924–1933.

[4]Jordan, P. F., "Vibration Study of a Pressurized Torus Shell, Part I—Experimental Study," NASA CR-884, Oct. 1967.

[5]Liepins, A. A., "Vibration Study of a Pressurized Torus Shell, Part II—Development and Applications of Analysis," NASA CR-885, Oct. 1967.

[6]Li, X., and Steigmann, D. J., "Finite Deformation of a Pressurized Toroidal Membrane," *International Journal of Non-Linear Mechanics*, Vol. 30, No. 4, 1995, pp. 583–595.

[7]Wolfram, S., *Mathematica, A System for Doing Mathematics by Computer*, Addison–Wesley, Reading, MA, 1991.

[8]Raouf, R. A., and Palazotto, A. N., "Nonlinear Dynamics of Unidirectional, Fiber-Reinforced Tori," *Journal of Engineering Mechanics*, Vol. 122, No. 3, 1996, pp. 271–276.

[9]Boresi, A. P., and Chang, K. P., *Elasticity in Engineering Mechanics*, Elsevier Science, New York, 1987.

[10]Gibson, R. F., *Principles of Composite Materials Mechanics*, McGraw–Hill, New York, 1994.

[11]Meirovitch, L., *Methods of Analytical Dynamics*, McGraw–Hill, New York, 1970.

[12]Brush, D. O., and Almroth, B. O., *Buckling of Bars, Plates, and Shells*, McGraw–Hill, New York, 1975.

[13]Reddy, J. N., *Energy and Vartiational Methods in Applied Mechanics*, Wiley-Interscience, New York, 1984.

[14]Timoshenko, S., and Woinowsky-Krieger, S., *Theory of Plates and Shells*, McGraw–Hill, New York, 1959.